Volume 28
Number 15
22 April 2026
Pages 8997–9814

PCCP

Physical Chemistry Chemical Physics

rsc.li/pccp

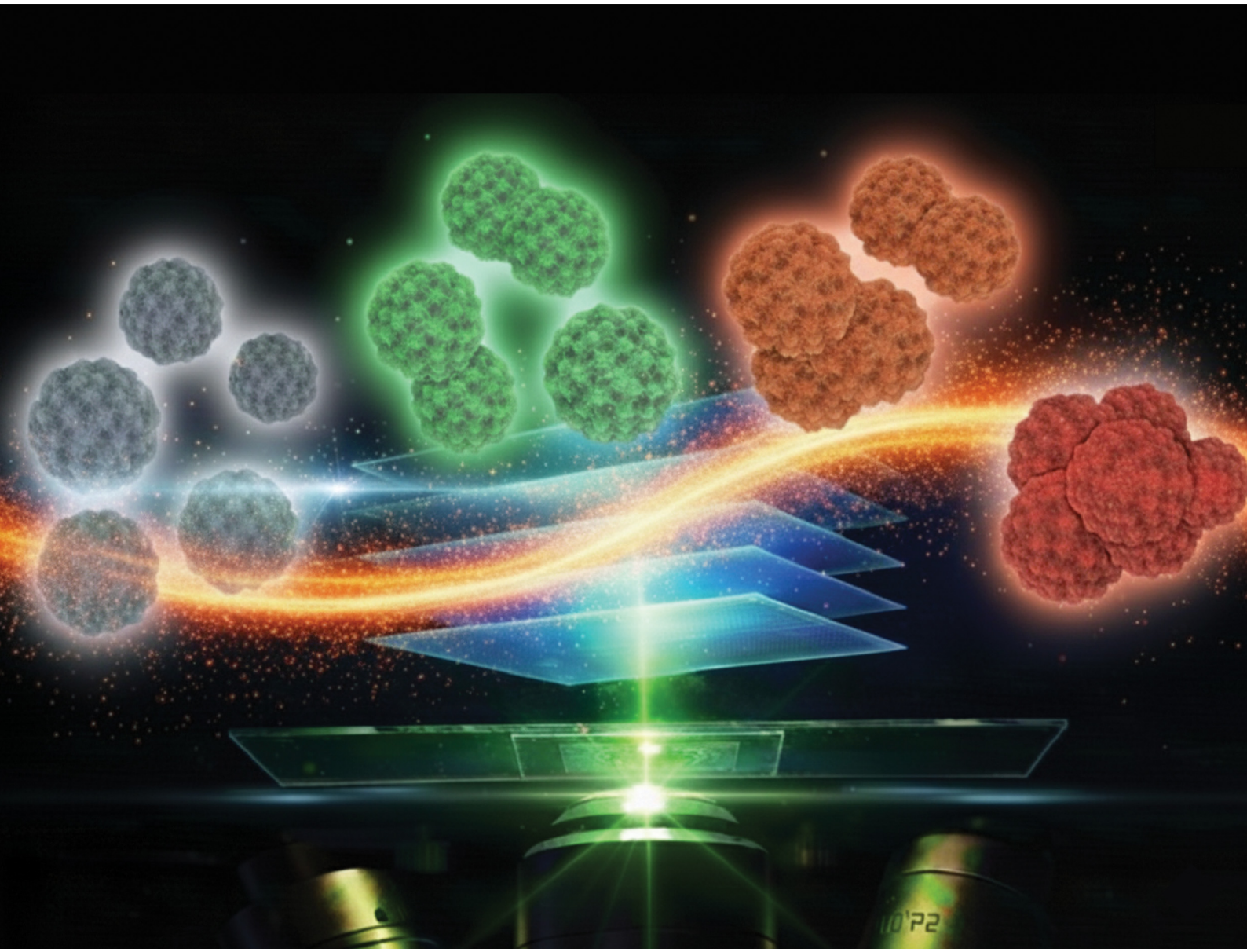

ISSN 1463-9076

ROYAL SOCIETY OF CHEMISTRY

PAPER

Jérôme J. Crassous, Ronald Gebhardt *et al.*
Probing the dynamics and stability of micellar casein and *para*-casein dispersions with differential dynamic microscopy

PCCP Owner Societies

PCCP

ROYAL SOCIETY OF CHEMISTRY

PAPER

View Article Online
View Journal | View Issue

Cite this: *Phys. Chem. Chem. Phys.*, 2026, **28**, 9172

Probing the dynamics and stability of micellar casein and *para*-casein dispersions with differential dynamic microscopy

Sebastian Thill, [a] Nabanita Hazra, [b] Meriem Saadli, [b] Frédéric Dux, [a] Jérôme J. Crassous *[bc] and Ronald Gebhardt *[a]

Received 1st November 2025,
Accepted 24th February 2026

DOI: 10.1039/d5cp04216j

rsc.li/pccp

Casein micelles and their rennet modification into *para*-casein micelles play a central role in the production of dairy products. They both hold great potential as functional materials in many applications from coatings to biomaterials, presenting a completely biological and sustainable alternative to petrochemicals. Regardless of their application, characterizing their dynamics, stability and ultimately their assembly is essential for their processing. In this study, casein- and *para*-casein micelle dispersions are characterized by differential dynamic microscopy (DDM). In contrast to conventional dynamic light scattering, DDM allows the characterization of highly turbid media and the simultaneous acquisition of the intermediate scattering function over a wide range of scattering vectors as illustrated by the investigation of concentrated casein micelle dispersions. We further demonstrate the application of this technique to investigate the colloidal stability of *para*-casein micelle dispersions, opening up for a potential use of this technique in the food industry and for diagnostic purposes.

1 Introduction

Casein is the main protein in milk and makes up to about 80% of the milk's total protein content. Due to their high proline content, caseins are generally described as a group of natively unfolded or intrinsically disordered proteins.[1] In bovine milk, four different genetic variations of caseins are present, namely α_{S1}-casein, α_{S2}-casein, β-casein and κ-casein. Together with calcium phosphate, they form complex association colloids referred to as casein micelles. The mean diameter of the micelles is between 100 nm and 150 nm and the micelles have a log normal size distribution between 50 nm and 500 nm.[2,3] At the casein micelle periphery, κ-casein builds up a so-called "hairy" layer. The hydrophilic C-terminal part expands into the surrounding solution, while the hydrophobic N-terminal part of the molecule is anchored inside the micelle. The so-formed κ-casein surface layer has a thickness of approximately 8 nm and stabilizes the micellar assembly by shielding further hydrophobic contacts.

From a technological perspective, the aggregation of casein micelles is of particular interest as it is often the base for gelled food products like yogurt or cheese.[4] Other applications involve microparticles to encapsulate bioactive substances[5,6] or regenerated protein fibers.[7] In their native form, the casein micelles are in a colloidal stable state. The κ-casein brush prevents aggregation *via* steric and electrostatic repulsion, *i.e.*, the micelles are kept far enough apart so that the repulsion forces dominate over the short-ranged van der Waals interactions.[4] In the primary phase of rennet coagulation, the rennet enzyme chymosin specifically cleaves the κ-casein at the Phe105–Met106 bond. This results in the release of the hydrophilic C-terminal part of the κ-casein while the hydrophobic N-terminal part remains attached to the micelle. The hydrolysed micelles are denoted as *para*-casein micelles (*p*-CMs) which, in the secondary phase of rennet coagulation, start to aggregate after about 80% of the κ-casein is hydrolysed.[8,9] The aggregation however only occurs when additional calcium ions are present and is strongly affected by temperature, pH and enzyme concentration.[4] Furthermore, the primary enzymatic phase and the secondary aggregation phase overlap and a precise description of the initial states during aggregation is difficult.[10] For example, while the radius of the micelles decreases due to hydrolysis and thus, *e.g.*, the turbidity of the sample decreases, the aggregation may already have started which causes an increase in turbidity.[10] Recently, image-based techniques have also been applied to investigate the early stages of milk gelation. Sekiguchi *et al.* employed mesoscopic image analysis to characterize the initial stages of glucono-δ-lactone-induced milk gelation, highlighting the potential of microscopy-based

[a] *Chair of Soft Matter Process Engineering (AVT.SMP), RWTH Aachen University, 52062 Aachen, Germany. E-mail: ronald.gebhardt@avt.rwth-aachen.de*
[b] *Institute of Physical Chemistry, RWTH Aachen University, Landoltweg 2, Aachen, DE-52074, Germany. E-mail: crassous@pc.rwth-aachen.de*
[c] *Jülich Centre for Neutron Science (JCNS-1), Forschungszentrum Jülich GmbH, 52425 Jülich, Germany*

approaches to access early aggregation dynamics in complex dairy systems.[11]

To study the enzymatic hydrolysis and coagulation independently, different approaches have been proposed. Carlson *et al.* used excess enzyme concentrations to complete the first step before the second step starts.[10,12] Dalgleish took advantage of the fact that aggregation of the micelles is almost completely inhibited at low temperatures.[13–15] Although the enzymatic hydrolysis is slow at low temperatures, it is not completely inhibited so that fully hydrolysed *p*-CMs can be prepared in a colloidal stable state when renneted in the cold. The aggregation can then be triggered by exposing the dispersion to a higher temperature. Extensive past research endeavors led to an increased understanding in the field of colloidal stability and several studies using different experimental approaches lead to a thorough understanding of the early stages of rennet induced coagulation. In 1983, Dalgleish studied the effect of temperature and calcium ion concentration on the stability of fully renneted casein micelles with turbidity measurements.[15] In 2014, Horne and Lucey revisited the data from Dalgleish and could determine an activation energy for the coagulation process and its intricate dependence on temperature and calcium content.[16] They postulated that the reduction of hydrophobic interactions, despite being substantial, is not the main reason for the inhibition of the coagulation process at low temperatures. Instead, an increase in electrostatic repulsion due to a weaker calcium binding to the micelle at lower temperatures was suggested to be the major contribution to the promoted stability of the dispersion. The diffusion-limited coagulation regime was identified at temperatures exceeding 50 °C, independent of the calcium content of the medium. Brinkhuis and Payens utilized static light scattering to investigate the coagulation of fully renneted casein micelles in the temperature range between 20 °C and 35 °C. The coagulation rate constant at 35 °C was measured to be 10.6×10^{-7} L mol^{-1} s^{-1} and was also observed to decrease at lower temperatures. The resulting activation energy in this temperature range was estimated at about 103 kJ mol^{-1}.[17] In our recent study, the coagulation of *p*-CMs was investigated with single particle tracking using fluorescence confocal microscopy. For this purpose, the CMs were first labeled with a fluorescent dye. After enzymatic treatment under non-aggregating conditions, coagulation was then triggered by a temperature jump. Evaluation of the tracking data showed that the coagulation process proceeds in two distinct steps. The formation and steady growth of aggregates could be first observed, which is followed by the abrupt formation a long-ranged gel network when the aggregates have reached a certain size.[18]

In this study, we introduce the use of differential dynamic microscopy (DDM) to study CM and *p*-CM dispersions. DDM is an emerging technique that probes the structure and dynamics of colloidal dispersions.[19] It offers the possibility to study challenging samples in different sample environments.[20] DDM is usually used to study colloids with particle sizes ranging from few tens of nanometres to micrometres.[19,21] A recent example includes the investigation of protein dispersions.[22] In particular, Safari *et al.* demonstrated that DDM can be applied to weakly scattering and polydisperse protein-rich clusters, establishing the applicability of the technique to soft and heterogeneous protein systems.[23] It can also be applied to probe the diffusion and mobility of biological active systems such as bacteria[24,25] or semen.[26] More recently, DDM has been extended to complex bio-nano systems, enabling *in situ* characterization of protein adsorption and aggregation processes both *in vitro* and *in vivo*.[27] It is worth noting that DDM is not restricted to bright field. For example, dense colloidal dispersions were investigated through DDM analysis in fluorescence confocal microscopy experiments[28] and the rotational dynamics of bacteria and colloidal clusters were examined using dark field imaging.[29] In contrast to conventional DLS, DDM can be applied to highly turbid colloidal dispersions[28–32] and allows the simultaneous determination of the dynamic and static properties of the sample.[28,33] DDM was also applied to flowing dispersions[34] and anisotropic colloids subjected to an external field[32,35] as the acquired 2D information allows one to distinguish the dynamics along different directions. Recently, two colour DDM enabled capturing dynamics faster than the camera framerate[36] and the application of spatial image windowing filters increased the accessible number of wave vectors.[37]

The purpose of this study is two-fold. First, we demonstrate that DDM can be successfully applied to complex biological dispersions, using concentrated casein micelle dispersions as a benchmark system. Second, we show that this technique can be used to quantitatively investigate the temperature-dependent stability and early-stage coagulation kinetics of dilute *para*-casein micelle dispersions by adapting the theoretical framework originally developed for combined dynamic and static light scattering.[38–40] In contrast to previous DDM studies on aggregation, the present work establishes a direct, experimentally validated correspondence between DDM-measured amplitudes and diffusion coefficients and absolute coagulation rate constants in an industrially relevant, functional protein system.

2 Theory

2.1 Differential dynamic microscopy (DDM)

DDM relies on the Fourier transform (FFT) of a time sequence of micrographs to obtain the power spectrum $g(q, \tau)$, where q refers to the wave vector of the fluctuations being probed and τ is the delay time between two frames recorded at a time $t + \tau$ and t, respectively. Considering the difference between the FFT of two frames

$$\widehat{\Delta I}(q, \tau) = I(q, t + \tau) - I(q, t), \quad (1)$$

the average power spectrum over τ can then be derived as follows:

$$g(q, \tau) = \left\langle \left| \widehat{\Delta I}(q, \tau) \right|^2 \right\rangle_t \quad (2)$$

By developing this expression, one obtains the fundamental equation of the DDM relating $g(q, \tau)$ to the intermediate scattering function $f(q, \tau)$:

$$g(q, \tau) = 2\left\langle |I(q, \tau)|^2 \right\rangle_t \left[1 - \frac{\langle I(q, t) I(q, t + \tau) \rangle_t}{\left\langle |I(q, t)|^2 \right\rangle_t} \right] \quad (3)$$

where $f(q, \tau)$ can be identified such that:

$$g(q, \tau) = A(q)[1 - f(q, \tau)] \quad (4)$$

The term $A(q)$ is here referred to as the amplitude and is proportional to the scattered intensity of the dispersion being probed. More precisely, $A(q)$ reflects the product of the sample-dependent scattering contribution, which includes the particle form factor and structure factor, and a q-dependent but time-independent optical transfer function $C(q)$ determined by the imaging conditions, as discussed in detail by Lu *et al.*[28] As a consequence, while the absolute value of $A(q)$ cannot be directly identified with the scattering intensity measured in static light scattering, its relative temporal evolution faithfully reflects changes in the scattered intensity. In addition, the τ-independent contribution of the dark count and read-out noise $B(q)$ must be added to eqn (4), leading to the final expression:

$$g(q, \tau) = A(q)[1 - f(q, \tau)] + B(q). \quad (5)$$

2.2 Coagulation kinetics

Focusing on the early stages of aggregation, the coagulation kinetics is based on the formation of particle dimers according to the following equation:[41]

$$A + A \rightarrow A_2 \quad (6)$$

The change in particle number concentration can be expressed as follows:[41,42]

$$\left.\frac{dN_1(t)}{dt}\right|_{t=0} = -k_{11}N_1^2(t) \quad (7)$$

$$\left.\frac{dN_2(t)}{dt}\right|_{t=0} = \frac{k_{11}N_1^2(t)}{2} \quad (8)$$

where $N_1(t)$ and $N_2(t)$ are the number densities of single particles and particles present in doublets, respectively, t is the coagulation time and k_{11} is the coagulation rate constant. In the literature, different techniques to measure k_{11} are discussed.[38–40]

In a static light scattering (SLS) experiment, the light scattering intensity $I(q)$ is recorded at different scattering wave vectors q corresponding to measurements performed at different scattering angles.

The intensity of the scattered light during the early stages of coagulation has only contributions from single particles and doublets. Defining the scattering of a single particle as $I_1(q)$ and the scattering of a particle in a doublet as $I_2(q)$, the total intensity is described by:[38]

$$I(q, t) = I_1(q)N_1(t) + I_2(q)N_2(t) \quad (9)$$

The rate of change of the scattered light is obtained from the derivation of eqn (9):

$$\frac{dI(q,t)}{dt} = I_1(q)\frac{dN_1(t)}{dt} + I_2(q)\frac{dN_2(t)}{dt} \quad (10)$$

k_{11} can then be derived by combining eqn (7), (8) and (10) using the initial derivative of intensity *versus* time normalized by the intensity at the onset of the coagulation $I(q, 0)$:

$$\left.\frac{1}{I(q,0)}\frac{dI(q,t)}{dt}\right|_{t\rightarrow 0} = k_{11}N_0\left(\frac{I_2(q)}{2I_1(q)} - 1\right) \quad (11)$$

Since the DDM amplitude is proportional to the scattered intensity through a q-dependent but time-independent transfer function, the normalized early-time variation of $A(q, t)$ is, in principle, expected to reflect the normalized variation of the scattering intensity. Accordingly, the coagulation rate constant extracted from the DDM amplitude should coincide with that obtained from static light scattering.

In the present work, we explicitly introduce a proportionality constant to account for the fact that DDM probes image intensity fluctuations rather than the scattered electric field directly, and that the definition of the DDM structure function involves specific numerical prefactors. This proportionality constant has not been introduced or discussed in previous studies and is included here to make explicit the correspondence between DDM-based and light-scattering-based analyses. We therefore write

$$\left.\frac{1}{A(q,0)}\frac{dA(q,t)}{dt}\right|_{t\rightarrow 0} = \alpha k_{11}N_0\left(\frac{I_2(q)}{2I_1(q)} - 1\right), \quad (12)$$

Here, the proportionality constant α explicitly defines the scaling relation between the DDM amplitude $A(q)$ and the single-particle scattering intensity $I(q)$. In particular, the DDM amplitude is not assumed to scale linearly with intensity, but instead follows a power-law relationship $A(q) = I(q)^{\alpha}$, where α is a dimensionless exponent that reflects the image-based nature of the DDM signal and the specific definition of the DDM structure function. Deviations from $\alpha = 1$ are expected due to the image-based definition of the DDM structure function, which relies on squared differences of Fourier-transformed image intensities rather than on direct measurements of scattering intensities. In practice, α was determined experimentally by comparing the coagulation rates obtained from amplitude-based and diffusion-based analyses under identical conditions.

In dynamic light scattering (DLS), intensity fluctuations of the scattered light are measured and quantified by the intensity correlation function. Under dilute conditions for purely diffusive systems, the decay rate $\Gamma(q, t)$ is related to the diffusion coefficient $D(q, t)$ as:

$$\Gamma(q, t) = -D(q, t)q^2 \quad (13)$$

The hydrodynamic radius $r_h(q, t)$ of the single particles and the aggregates can then be directly derived from $D(q, t)$ *via* the Stokes–Einstein equation:

$$r_h(q,t) = \frac{k_B T}{6\pi\eta D(q,t)} \quad (14)$$

where k_B is the Boltzmann constant, T is the temperature and η is the viscosity of the solution. It is important to note that during the coagulation process, the measured diffusion coefficient $D(q, t)$ is the intensity-weighted diffusion of the sum of the

single particles characterized by their diffusion coefficient and hydrodynamic radius, D_1 and $r_{h,1}$, and the doublets diffusion coefficient D_2 and $r_{h,2}$:

$$D(q,t) = \frac{N_1(t)I_1(q)D_1 + N_2(t)I_2(q)D_2}{N_1(t)I_1(q) + N_2(t)I_2(q)} \quad (15)$$

eqn (15) can be expressed as a function of the hydrodynamic radii as:

$$\frac{1}{r_h(q,t)} = \frac{1}{r_{h,1}r_{h,2}} \frac{r_{h,2}N_1(t)I_1(q) + r_{h,1}N_2(t)I_2(q)}{N_1(t)I_1(q) + N_2(t)I_2(q)} \quad (16)$$

The initial relative variation of the hydrodynamic radius is then obtained by deriving eqn (16) as a function of t:

$$\frac{1}{r_h(q,0)} \frac{\mathrm{d}r_h(q,t)}{\mathrm{d}t}\bigg|_{t\to 0} = \frac{I_2(q)}{2I_1(q)}\left(1 - \frac{r_{h,1}}{r_{h,2}}\right)k_{11}N_0 \quad (17)$$

To calculate the coagulation rate constant (CRC) from eqn (11) and (17), respectively, the so-called optical factor $I_2(q)/(2I_1(q))$ needs to be calculated. According to the Rayleigh–Gans–Debye (RGD) theory, the optical factor can be expressed as follows:

$$\frac{I_2(q)}{2I_1(q)} = 1 + \frac{\sin(2qr_{h,1})}{2qr_{h,1}} \quad (18)$$

The RGD approximation is only valid for small particles. With increasing particle size and higher refractive index, the approximation is no longer valid. In order to determine k_{11} independently of the optical factor, Holthoff *et al.* suggested combining eqn (11) and (17). This approach is referred to as simultaneous static and dynamic light scattering (SSDLS):[38]

$$k_{11}N_0 = \frac{1}{r_h(q,0)}\left(1 - \frac{r_{h,1}}{r_{h,2}}\right)^{-1} \frac{\mathrm{d}r_h(q,t)}{\mathrm{d}t}\bigg|_{t\to 0} - \frac{1}{I(q,0)} \frac{\mathrm{d}I(q,t)}{\mathrm{d}t}\bigg|_{t\to 0} \quad (19)$$

Which in the case of the DDM measurement leads to the following equation:

$$k_{11}N_0 = \frac{1}{r_h(q,0)}\left(1 - \frac{r_{h,1}}{r_{h,2}}\right)^{-1} \frac{\mathrm{d}r_h(q,t)}{\mathrm{d}t}\bigg|_{t\to 0} - \frac{1}{\alpha A(q,0)} \frac{\mathrm{d}A(q,t)}{\mathrm{d}t}\bigg|_{t\to 0} \quad (20)$$

The stability of the dispersion is described by the stability ratio W, *i.e.*, the ratio of the fast, diffusion-limited coagulation rate k_{fast} and k_{11}:

$$W = \frac{k_{fast}}{k_{11}} \quad (21)$$

where k_{fast} is expressed with the Smoluchowski diffusion-limited rate:

$$k_{fast} = \frac{8k_BT}{3\eta} \quad (22)$$

Ultimately, W reflects the interparticle interaction potential and the balance between attractive and repulsive interactions.[38] Under the current investigation, the increased attractive interactions between p-CMs with the temperature can be captured by an activation energy V_{max} determined from the Arrhenius-like dependence of W as a function of T:[16,43]

$$W \approx (2\kappa r_{h,1})^{-1} \exp\left(\frac{V_{max}}{k_BT}\right) \quad (23)$$

where the inverse Debye length κ characterizes the electric double layer and V_{max} is the height of the repulsive energy barrier. When rewriting eqn (23), the activation energy in units of k_B can be extracted from the slope of the Arrhenius plot of $\ln W$ over the reciprocal temperature $1/T$.

3 Materials

The casein micelles used in this study were isolated from fresh whole milk, obtained from a local dairy farm (Soerser Milchkännchen, Aachen, Germany). In a first centrifugation step at 3000 × RCF for 20 min, the milk was skimmed before the casein micelles are isolated in a second ultracentrifugation step at 70 000 × RCF for 60 min using an Optima XP-80 ultracentrifuge (Beckman Coulter GmbH, Krefeld, Germany). The supernatant was removed, and the remaining casein pellet was redispersed in the simulated milk ultrafiltrate (SMUF) by stirring for 2 h at 37 °C. The SMUF buffer was prepared according to the procedure described in ref. 44. To prevent microbial growth, 0.05% (w/w) sodium azide (99%, Carl Roth, Karlsruhe, Germany) was added. The CM concentration was measured gravimetrically and adjusted to the desired concentration by dilution with SMUF. For cold renneting, the solution was incubated with the 50 IMCU L^{-1} rennet enzyme (CHY-MAX M, Chr. Hansen A/S, Hoersholm, Denmark) at 5 °C for 24 h, resulting in a stable p-CM dispersion.

4 Methods

4.1 DDM measurements

DDM was performed in brightfield mode using an inverted Nikon TE300 microscope equipped with a 40× Plan Apo objective (Nikon CFI P-Apo Lambda NA = 0.95). Image stacks were recorded using a monochrome USB3 FLIR Blackfly@ camera (720 × 520 resolution). In a typical procedure, 10.000 256 × 256 pixel^2 frames (pixel size = 1.75 × 10^{-7} m) were captured with a framerate of 997 fps. The temperature was ensured using a thermostated enclosure from Okolab. For measurements, 7.5 μL of the CM or p-CM dispersion were placed in the center of a spacer (Secure-SealTM imaging spacer, diameter × thickness: 13 mm × 0.12 mm, Thermo-Fischer) on a cover slide with a thickness of 170 μm (Corning® borosilicate glass, $W \times L$ 24 mm × 60 mm, Sigma-Aldrich) and then sealed with another cover slide. The focus was adjusted so that the focal plane was in the center of the sample at a z-depth of 60 μm. DDMSoft (github.com/duxfrederic/ddmsoft), a Python based GUI, was used to convert the microscopy videos into the DDM matrix and perform multi wavenumber data analysis.

For the measurements on CM dispersions, each experiment was repeated five times under identical conditions. The reported

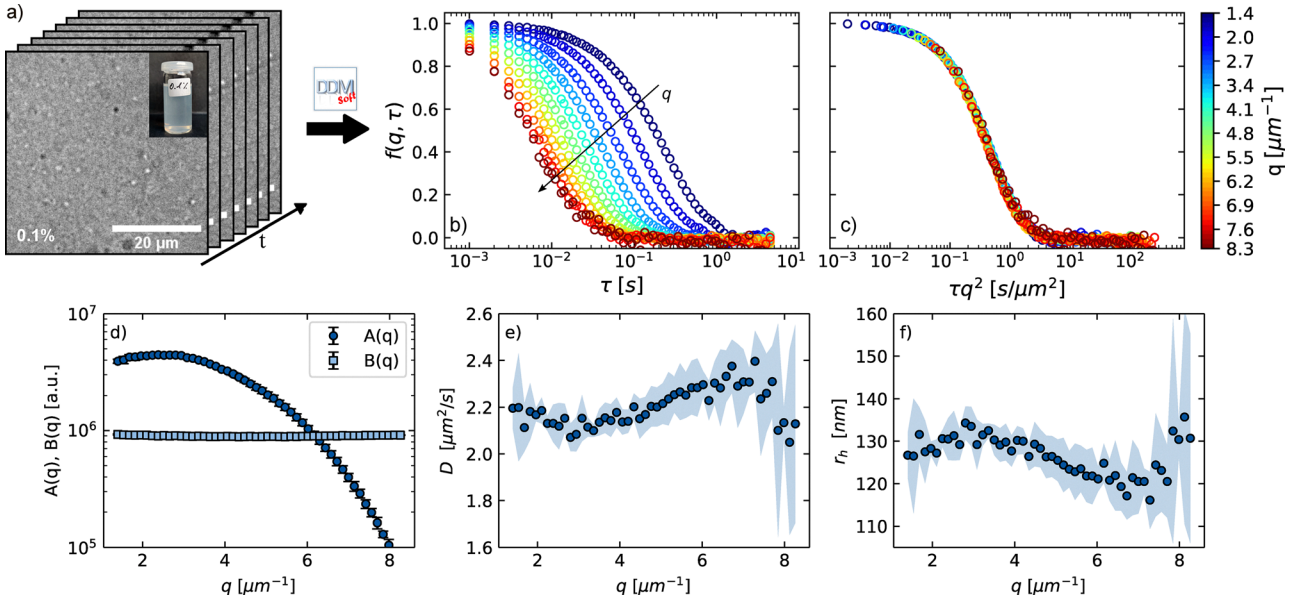

Fig. 1 (a) Micrograph stack of a 0.1% (w/w) CM dispersion at T = 20 °C. (b) Intermediate scattering function $f(q, \tau)$ extracted from the image stack using DMMSoft at various q over τ and (c) at various q, rescaled as a function of τq^2. (d) Amplitude $A(q)$ and noise $B(q)$ over q. (e) Diffusion coefficient obtained *via* second order cumulant analysis and (f) hydrodynamic radius as function of q.

values on a dilute CM dispersion reported in Fig. 1 correspond to the mean of these independent measurements, and the associated error bars represent the corresponding standard deviations. For the concentration-dependent measurements shown in Fig. 2, the DDM analysis was performed on averaged correlation functions, and the diffusion coefficients were obtained by averaging over the relevant q-range. In this case, the error bars represent the standard deviation of the q-averaged quantities. For the time-dependent coagulation experiments on *para*-casein micelles, DDM measurements were performed continuously after triggering aggregation by a temperature jump. Image stacks were recorded sequentially on the same sample, allowing the evolution of both the DDM amplitude and the intermediate scattering function to be monitored as a function of time. Due to experimental constraints related to sample preparation and the limited time window during which comparable coagulation conditions could be maintained, these temperature-dependent coagulation experiments were performed once for each temperature.

4.2 Viscosimetry

Viscosity measurements were performed using a Lovis 2000 viscosimeter (Anton Paar, Austria). The zero-shear rate viscosity was determined by extrapolating the measured values at 5 different angles and relating them to the viscosity of the solvent (SMUF-Buffer) to obtain the relative viscosity.

5 Results and discussion

5.1 Characterization of the casein micelle dispersions

DDM measurements were performed on a 0.1% (w/w) CM dispersion at a T of 20 °C. Fig. 1a displays a stack of the acquired brightfield micrographs. Due to their scattering, CMs appear as randomly diffusing particles, although their actual size is below the diffraction limit. We use DDMSoft to compute the DDM based on 300 couples of frames and 20 considered lag times τ per decade of measured time. The $f(q, \tau)$s plotted in Fig. 1b are derived from a second cumulant analysis of the $g(q, \tau)$s performed between q= 1.40 µm^{-1} and 8.26 µm^{-1}. As shown in Fig. 1c, the $f(q, \tau)$s can be rescaled into a master curve when plotted against τq^2 attesting for the diffusive character of the CM dispersion. The amplitude $A(q)$ is, up to q = 6 µm^{-1}, larger than the noise $B(q)$ which indicates a sufficient signal to noise ratio of the 0.1% (w/w) dispersion in this q-range. $A(q)$ shows a maximum at low q and decreases for larger q. As pointed out earlier, $A(q)$ is related to the scattering intensity of the sample and contains contributions from the particle form factor and structure factor coupled by a transfer function. Further details on the transfer are discussed in ref. 45 and are beyond the scope of this study. $B(q)$ is almost constant over q as the camera adds mainly white noise.[46] The diffusion coefficients plotted in Fig. 1e slightly increase by about 10% from *circa* 2.1 to 2.3 µm^2 s^{-1} with increasing q. We ascribe this effect to the polydispersity of the sample as larger CMs contribute more to the signal at low q as reported from light scattering studies.[47] The q-dependence of the hydrodynamic radius can be estimated from the diffusion coefficients *via* the Stokes–Einstein relationship (eqn (14)). r_h averaged over q = 2–6 µm^{-1} was determined to be 126 ± 5 nm in good agreement with literature values.[2,3] Comparable results were obtained from a first cumulant analysis (Fig. S1) or by fitting with a stretched exponential (Fig. S2), as discussed in the SI.

5.2 Concentrated casein micelle dispersions

As mentioned earlier, conventional DLS is usually limited to non-turbid media. The following experiments demonstrate that DDM can be applied to the investigation of concentrated CM

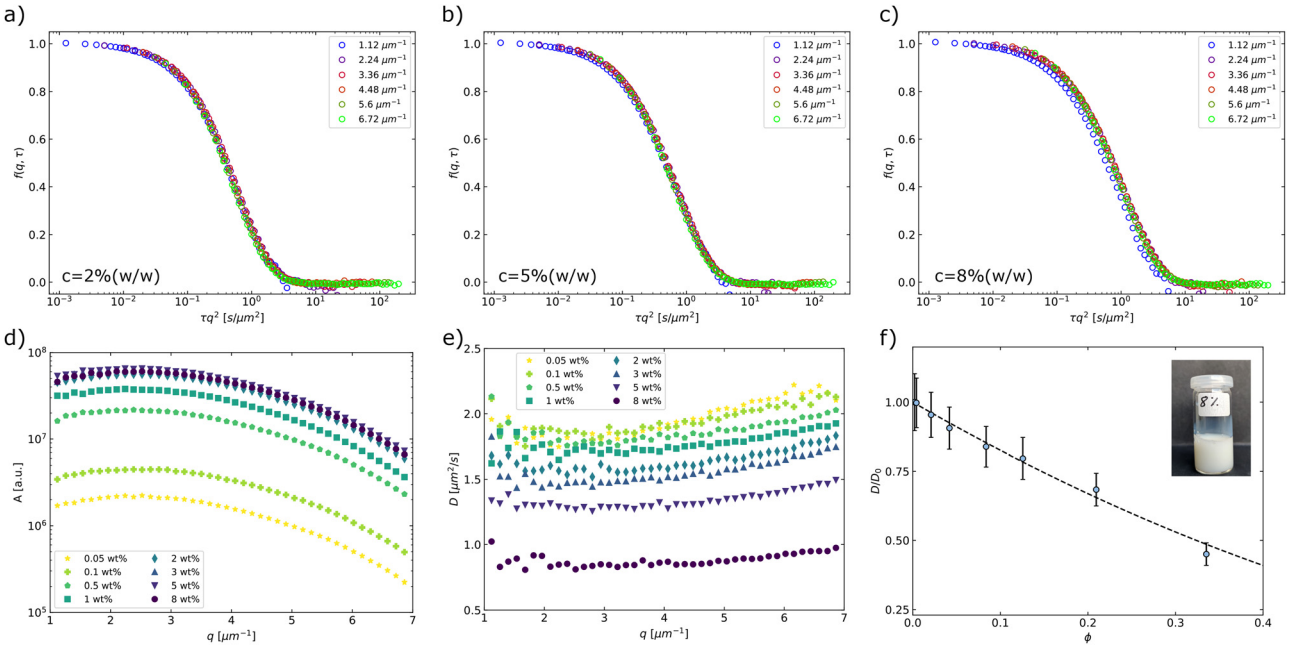

Fig. 2 (a)–(c) Averaged intermediate scattering functions for the CM dispersions at different concentrations. (d) q-Dependent DDM amplitude $A(q)$ for different concentrations. (e) Diffusion coefficient as a function of q for different concentrations. (f) Normalized diffusion coefficient D/D_0 averaged over q = 2–6 μm^{-1}. The dots represent the measured values with error bars indicating the standard deviation of the q-average. The dashed line corresponds to the theoretical value obtained by the Beenakker–Manzur formalism for hard spheres calculated with eqn (24). The inset displays the highly turbid sample at c = 8% ($\phi \approx 0.33$).

dispersions. For this purpose, a concentration series of CM dispersions ranging from 0.05 to 8% (w/w) was prepared and measured at 30 °C. The volume fraction of the CM suspensions was estimated *via* viscosimetry using the Batchelor–Einstein equation $\eta_r = 1 + 2.5kc + 6.2(kc)^2$, where η_r is the relative viscosity, k is the voluminosity in mL g^{-1}, and c is the concentration in g mL^{-1}. The voluminosity was found to be 4.19 mL g^{-1}, which is in good agreement with the value reported in the literature.[48]

The $f(q, \tau)$ functions shown in Fig. 2a–c exhibit a single relaxation process that shifts to longer times with increasing concentration. The $f(q, \tau)$ were fitted with a stretched exponential to estimate diffusion coefficients averaged over q, with stretched exponents varying between approximately 0.9 and 0.8. The measured diffusion corresponds to the slow collective diffusion of the CMs, which dominates the signal.

It is well known that colloidal systems undergo a dynamic slowing down with increasing concentration, ultimately approaching an arrested state near the colloidal glass transition.[49,50] Although the measurements shown here at a volume fraction of ϕ = 0.33 are still far from the critical packing density ϕ_c = 0.69 reported by Dahbi *et al.*,[51] interparticle interactions are no longer negligible and the diffusion of individual micelles is increasingly hindered due to crowding.

Fig. 2d shows the amplitude $A(q)$ extracted from the DDM fits for different CM concentrations. At low concentrations, up to approximately 0.1 wt%, $A(q)$ scales proportionally with concentration, consistent with the dilute regime where interparticle interactions are negligible. At higher concentrations, this proportionality no longer holds, reflecting the increasing role of interparticle interactions and static correlations, which affect the image-based DDM amplitude. Consequently, $A(q)$ cannot be interpreted as a direct measure of concentration in this regime, while the dynamic information extracted from the decay of $f(q, \tau)$ remains unaffected.

At these higher concentrations, the measured diffusion coefficients can no longer be employed to determine r_h since the Stokes–Einstein equation applies to the diffusion coefficient D_0 in the high-dilution limit, which in our case corresponds to measurements performed at 0.1% (w/w). However, the CM diffusion coefficient $D(\phi)$ has been reported to follow hard-sphere behavior up to a volume fraction ϕ = 0.2.[47,52] Accordingly, $D(\phi)$ can be described by the Beenakker–Mazur formalism:[52–55]

$$D(\phi)/D_0 = 1 - 1.83\phi + 0.88\phi^2 \quad (24)$$

To test this relationship, Fig. 2f compares the measured diffusion coefficients, normalized to D_0, with eqn (24). Our measurements show that the CMs follow hard-sphere behavior over the entire investigated range of up to ϕ = 0.33. Therefore, we conclude that DDM can be applied to the investigation of concentrated and highly turbid CM dispersions.

5.3 Coagulation kinetics of *p*-CMs

The coagulation of dilute, 0.1% (w/w), dispersions of fully renneted *p*-CMs at different temperatures between 30 °C and 45 °C was followed *via* DDM. Measurements were taken every 20 s allowing the temporal evolution of the hydrodynamic radius and the DDM amplitude at different q-values to be followed as shown in Fig. 3. The radius of the CMs before the

onset of the coagulation process was found around 150–170 nm with a tendency to increase at higher temperatures. At 45 °C, the r_h increases rapidly from 170 nm to 600 nm in about 400 s. The drop in r_h after 400 s is ascribed to the sedimentation of the large aggregates. With decreasing temperature, the coagulation process slows down and at 30 °C, no significant coagulation takes place within the considered time interval of 2 h. A slight q-dependence is visible for r_h, which is more pronounced at higher temperatures. The aggregation is also accompanied by an increase in the scattering intensity, captured by the increase of $A(q, t)$. The amplitude has pronounced q-dependence as illustrated by the evolution of the normalized amplitude shown in Fig. S5. Similar to r_h measurements, at low temperatures, $A(q, t)$ is almost constant which indicates that no significant coagulation takes place.

To calculate k_{11} in the dilute regime, the focus is set on the initial stages of the coagulation. The initial slopes of the radius and amplitude are derived from a linear fit to the data at the start of the coagulation. Therefore, to match the onset of coagulation, the coagulation time is shifted by a lag time t_0, which decreases at higher temperatures. The fit interval t_{fit} is set individually for each temperature. The parameters and the initial averaged $r_h(t_0)$ are listed in Table 1. The initial number density of micelles N_0 was calculated according to the following equation:

$$N_0 = \frac{3kc}{4\pi r_h(t_0)^3} \quad (25)$$

Table 1 Early-stage hydrodynamic radius and characteristic times extracted from DDM

T (°C)	t_0 (s)	r_h (t_0) (nm)	std($r_h(t_0)$) (nm)	t_{fit} (s)
30	1166	173.2	7.9	7445
35	437	141.3	6.1	2155
36	329	161.0	13.4	794
37	144	154.0	9.8	528
38	119	170.5	15.5	276
39	72	159.8	12.0	250
40	63	165.0	9.0	211
45	22	171.5	9.0	126

where c is the initial concentration in % (w/w) and the voluminosity k is from the casein micelles corrected for the different temperatures.

Fig. 4a displays the normalized initial slopes of the hydrodynamic radius and Fig. 4b displays the DDM amplitude over q obtained by the linear fit to the onset of the aggregation curves for each temperature. For all temperatures, the slopes decrease with increasing q. This behavior is consistent with eqn (11) and (18), as the normalized scattering intensity (and correspondingly the DDM amplitude) is expected to scale with $\sin(2qr_{h,1})/(2qr_{h,1})$. For a characteristic hydrodynamic radius $r_{h,1} \approx 150$ nm, this term decreases by approximately 40% between $q = 2$ μm^{-1} and $q = 6$ μm^{-1}. In addition, the intrinsic polydispersity of the casein micelle suspension is expected to contribute to this trend, as

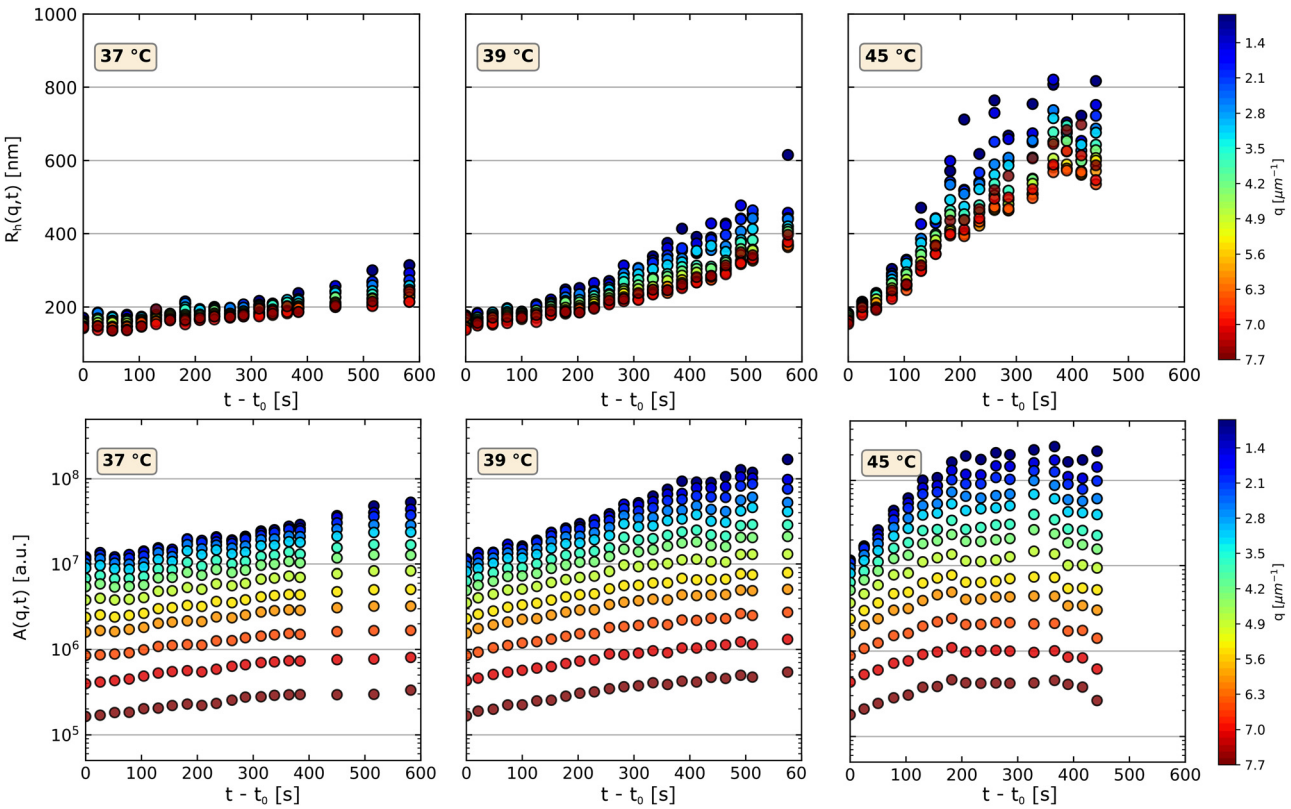

Fig. 3 Temporal evolution of the hydrodynamic radius (top) and the DDM amplitude $A(q)$ (bottom) during the aggregation of the *para*-casein micelles for selected temperatures (37 °C, 39 °C, and 45 °C). The full data set is provided in the SI.

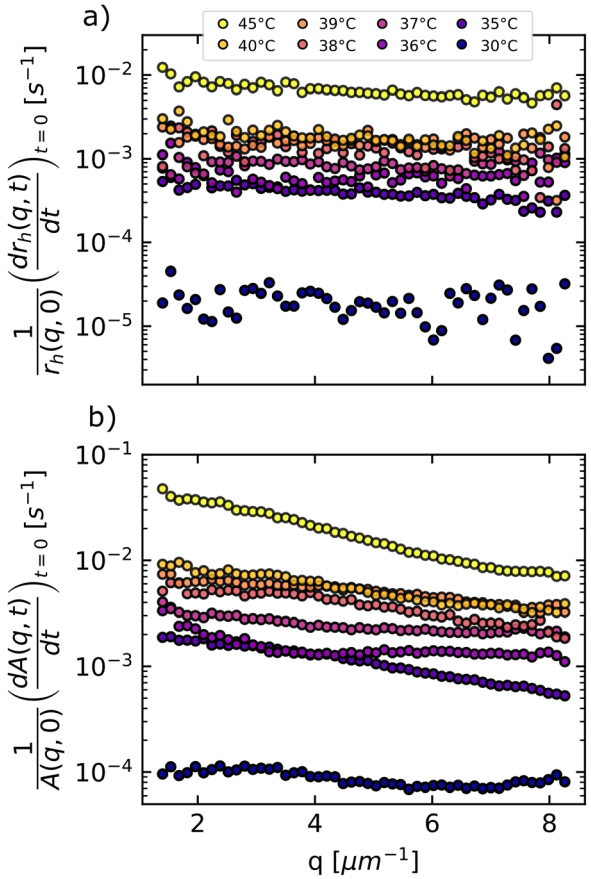

Fig. 4 Normalized initial slopes of (a) the hydrodynamic radius and (b) the DDM amplitude calculated from a linear fit to the onset of the aggregation curves.

particles of different sizes contribute differently to the DDM signal at different wave vectors (see Fig. S5).

Furthermore, as expected, the slopes increase with increasing temperature and the rate of change for both the hydrodynamic radius and the DDM amplitude are over one order of magnitude lower at 30 °C when compared to 35 °C. As described earlier, the coagulation rate constant k_{11} can be calculated *via* different approaches, *i.e.*, *via* static light scattering, dynamic light scattering or a combined approach which is referred to as simultaneous static and dynamic light scattering (SSDLS). Assuming that the *para*-CMs do not deform, in the static and dynamic calculations, the required information about the optical properties of the particle monomers and dimers can be calculated using the RGD approximation. In the SSDLS approach, the coagulation rate becomes independent on the doublet form factor. However, $r_{h,2}$ is still required. At low concentrations, casein micelles are considered as hard spheres[47,52] for which the hydrodynamic radius of the particle doublets is about 1.38 times the monomer radius.[38] We use the initial slopes taken from the onset of the aggregation curves and eqn (12), (17) and (20) to determine $k_{11}N_0$.

The correspondence between DDM-based and scattering-based determinations of the coagulation rate constant involves a proportionality factor α. This factor was determined by minimizing the difference between the values of $k_{11}N_0$ obtained from three independent approaches, namely static light scattering, dynamic light scattering, and their combined SSDLS analysis. The resulting values of α are summarized in Table 2. Within experimental uncertainty, α clusters around a mean value of $\alpha = 2.10 \pm 0.4$ and shows no systematic dependence on temperature. Given this consistency, and since the mean value is close to $\alpha = 2$, we use $\alpha = 2$ as a representative value in the following analysis. The results obtained with this choice are presented in Fig. 5. Using $\alpha = 2.10$ instead of $\alpha = 2$ changes the absolute values of k_{11} only within the experimental uncertainty and does not affect the observed temperature dependence or the extracted stability ratios.

Table 2 Determination of the α-parameter from the analysis of the coagulation rate constant determined by static light scattering, dynamic light scattering and the combination of the two techniques (SSDLS)

T (°C)	α (−)
30	2.89
35	1.91
36	1.65
37	1.99
38	1.97
39	2.22
40	2.05
45	2.24

A plot of $k_{11}N_0$, derived from the three different approaches, is shown in Fig. 5a–c for selected aggregation temperatures. As expected, the aggregation rate increases with increasing temperature. At 37 °C and 39 °C, the coagulation rate constants show almost no q-dependence and similar values for each of the calculation methods. At 45 °C, the q-dependence of the coagulation rate constant is much more pronounced than at lower temperatures and the average value is 3–4 times higher compared to the aggregation at 39 °C. We assume that the q-dependence of the coagulation rate is mainly caused by the large q-dependence in the initial slope of the DDM amplitude shown in Fig. 4b. Fig. 5d shows the q-averaged initial hydrodynamic radius $r_h(t_0)$ of the single p-CMs, as a function of the aggregation temperature. The error bars represent the standard deviation from averaging over q. At low temperatures, the $r_h(t_0)$ value is between 140 nm and 150 nm and increases with increasing aggregation temperature. At 45 °C the initial micellar radius is found to be about 170 nm. Previous SLS high-pressure experiments have shown that the structural stability of the micelles increases in the range between 30 and 50 °C.[56] The increase in stability can be explained by the stronger binding of β-casein chains within the micelle composite and is associated with an increase in the hydrodynamic radius, as shown by *in situ* DLS high-pressure experiments.[57] While the internal stability of p-CMs increases with increasing temperature similar to native casein micelles, the aggregation ability in contrast also increases for the renneted micelles. In Fig. 5e, the stability ratio W is plotted against T.

The static, dynamic and SSDLS calculation method led to comparable results. At 30 °C, the p-CM dispersion was almost stable as no significant aggregation took place over a time of 2 h, leading to the high value of W. With increasing T, the aggregation becomes faster, leading to a marked decrease of W. No plateau

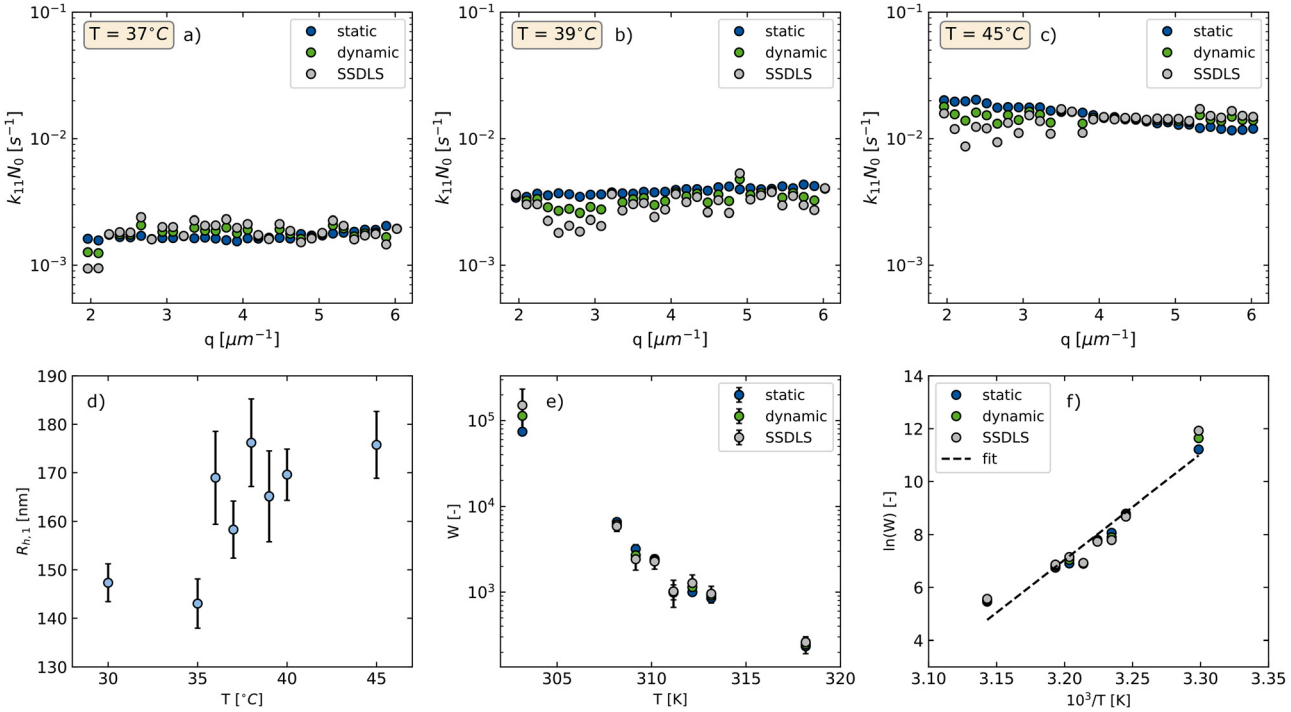

Fig. 5 (a)–(c) Coagulation rate constant $k_{11}N_0$ for selected aggregation temperatures (37 °C, 39 °C and 45 °C), calculated using the static, dynamic and the SSDLS approach. (d) q-Averaged hydrodynamic radius of the particle monomers at different aggregation temperatures. (e) q-Averaged stability ratio as a function of aggregation temperature. (f) W plotted in an Arrhenius representation as a function of $1/T$. The linear fit to the data (dashed line) allows for the determination of V_{max}.

value could be observed in the investigated temperature range indicating that the fast diffusion regime has not yet been reached. In other studies, the fast aggregation regime, *i.e.*, the temperature regime where the stability ratio is independent of the aggregation temperature was found to start at about 50 °C, depending on the ionic strength of the sample.[15,16] In Fig. 5f, W is plotted as a function of T following an Arrhenius representation. According to eqn (24), the height of the repulsive energy barrier, V_{max} = 332 kJ mol^{-1}, is obtained from the slope of the data. We found this value to be significantly higher than previously reported values, measured using SLS at higher dilutions.[17] In the experiments in ref. 17, the influence of the renneting process on the aggregation rate possibly could not be excluded. This might explain the comparatively low activation energy and the original conclusion that the micelles adhere *via* hydrophobic bonding. The authors in ref. 17 also concluded that the aggregation rates are independent of the size of the micelles, a finding that appears to be confirmed by our results.

6. Conclusions

Beyond the specific case of casein micelles, the present results illustrate how differential dynamic microscopy can be used to quantitatively access aggregation kinetics and stability ratios in complex colloidal protein systems using a single experimental framework. In particular, the ability to extract absolute coagulation rate constants from both amplitude-based and diffusion-based analyses, and to explicitly assess their correspondence, highlights the potential of DDM to complement or replace conventional scattering techniques in situations where the sample volume is limited or the turbidity is high.

The systematic proportionality factor identified between the DDM amplitude and the scattering intensity further points to an important methodological aspect that deserves attention in future studies and should be tested across a broader range of synthetic and biological colloidal systems. In this sense, DDM offers not only a practical experimental tool, but also a platform for critically examining how image-based measurements relate to traditional scattering techniques.

These features make DDM particularly attractive for studying aggregation and stability phenomena in industrial, food, and biomedical contexts, where early-stage clustering and subtle changes in colloidal interactions often play a decisive role. In particular, the low sample volume requirement and experimental accessibility of DDM suggest its use as a complementary technique in the formulation and characterization of industrial dispersions, including food and cosmetic systems. Similar considerations apply in biomedical contexts, where image-based approaches may contribute to the study of aggregation-related processes relevant to thrombosis, antigen detection, and neurodegenerative diseases.[58–60]

Author contributions

The manuscript was written through contributions of all authors. The experiments and data evaluation were performed

by ST and NH. FD is at the origin of the DDMSoft software used for the data evaluation. All authors have given approval to the final version of the manuscript.

Conflicts of interest

There are no conflicts to declare.

Data availability

The data supporting this study, including the DDM matrices, their analysis performed using the DDMsoft software (https://github.com/duxfrederic/ddmsoft), and the corresponding viscosimetry data, are available from Zenodo at https://doi.org/10.5281/zenodo.18313639.

Supplementary information (SI) is available. See DOI: https://doi.org/10.1039/d5cp04216j.

Acknowledgements

The authors acknowledge financial support from the Exploratory Research Space of RWTH Aachen University for the research project (BioTrans012) and for the development of the DDM platform (project StUpJP-049-18).

References

1 H. M. Farrell, P. X. Qi and V. N. Uversky, *Advances in Biopolymers*, American Chemical Society, 2006, pp. 52–70.
2 C. G. de Kruif and C. Holt, *Advanced Dairy Chemistry–1 Proteins*, Springer, US, 2003, pp. 233–276.
3 P. F. Fox and A. Brodkorb, *Int. Dairy J.*, 2008, **18**, 677–684.
4 M. Corredig and E. Salvatore, *Advanced Dairy Chemistry*, Springer, New York, 2016, pp. 287–307.
5 T. Heidebach, P. Först and U. Kulozik, *Food Hydrocolloids*, 2009, **23**, 1670–1677.
6 J. Schulte, M. Stöckermann, S. Thill and R. Gebhardt, *Int. Dairy J.*, 2020, **105**, 104692.
7 S. Thill, T. Schmidt, D. Wöll and R. Gebhardt, *Colloid Polym. Sci.*, 2021, **299**, 201–210.
8 D. G. Dalgleish, *J. Dairy Res.*, 1979, **46**, 653–661.
9 R. Tuinier and C. G. de Kruif, *J. Chem. Phys.*, 2002, **117**, 1290–1295.
10 M. S. Pires, C. A. Gatti, G. A. Orellana and J. Pereyra, *J. Agric. Food Chem.*, 1997, **45**, 4446–4451.
11 K. Sekiguchi, M. Tanimoto and S. Fujii, *Gels*, 2023, **9**, 202.
12 A. Carlson, C. G. Hill and N. F. Olson, *Biotechnol. Bioeng.*, 1987, **29**, 590–600.
13 N. Bansal, P. F. Fox and P. L. H. McSweeney, *J. Agric. Food Chem.*, 2007, **55**, 3120–3126.
14 P. Walstra, *J. Dairy Sci.*, 1990, **73**, 1965–1979.
15 D. G. Dalgleish, *J. Dairy Res.*, 1983, **50**, 331–340.
16 D. S. Horne and J. A. Lucey, *Food Hydrocolloids*, 2014, **42**, 75–80.
17 J. Brinkhuis and T. A. Payens, *Biophys. Chem.*, 1984, **19**, 75–81.
18 S. Thill, T. Schmidt, D. Wöll and R. Gebhardt, *Int. Dairy J.*, 2020, **105**, 104659.
19 R. Cerbino and V. Trappe, *Phys. Rev. Lett.*, 2008, **100**, 188102.
20 R. Cerbino, F. Giavazzi and M. E. Helgeson, *J. Polym. Sci.*, 2022, **60**, 1079–1089.
21 D. Germain, M. Leocmach and T. Gibaud, *Am. J. Phys.*, 2016, **84**, 202–210.
22 C. Guidolin, C. Heim, N. B. P. Adams, P. Baaske, V. Rondelli, R. Cerbino and F. Giavazzi, *Macromolecules*, 2023, **56**, 8290–8297.
23 M. S. Safari, M. A. Vorontsova, R. Poling-Skutvik, P. G. Vekilov and J. C. Conrad, *Phys. Rev. E*, 2015, **92**, 042712.
24 L. G. Wilson, V. A. Martinez, J. Schwarz-Linek, J. Tailleur, G. Bryant, P. N. Pusey and W. C. K. Poon, *Phys. Rev. Lett.*, 2011, **106**, 018101.
25 V. A. Martinez, R. Besseling, O. A. Croze, J. Tailleur, M. Reufer, J. Schwarz-Linek, L. G. Wilson, M. A. Bees and W. C. K. Poon, *Biophys. J.*, 2012, **103**, 1637–1647.
26 A. Jepson, J. Arlt, J. Statham, M. Spilman, K. Burton, T. Wood, W. C. K. Poon and V. A. Martinez, *PLoS One*, 2019, **14**, e0202720.
27 P.-L. Latreille, J.-M. Rabanel, M. Le Goas, S. Salimi, J. Arlt, S. A. Patten, C. Ramassamy, P. Hildgen, V. A. Martinez and X. Banquy, *Adv. Mater.*, 2022, **34**, 2203354.
28 P. J. Lu, F. Giavazzi, T. E. Angelini, E. Zaccarelli, F. Jargstorff, A. B. Schofield, J. N. Wilking, M. B. Romanowsky, D. A. Weitz and R. Cerbino, *Phys. Rev. Lett.*, 2012, **108**, 218103.
29 R. Cerbino, D. Piotti, M. Buscaglia and F. Giavazzi, *J. Phys.: Condens. Matter*, 2018, **30**, 025901.
30 T. Sentjabrskaja, E. Zaccarelli, C. de Michele, F. Sciortino, P. Tartaglia, T. Voigtmann, S. U. Egelhaaf and M. Laurati, *Nat. Commun.*, 2016, **7**, 11133.
31 M. Laurati, T. Sentjabrskaja, J. Ruiz-Franco, S. U. Egelhaaf and E. Zaccarelli, *Phys. Chem. Chem. Phys.*, 2018, **20**, 18630–18638.
32 A. Pal, V. A. Martinez, T. H. Ito, J. Arlt, J. J. Crassous, W. C. K. Poon and P. Schurtenberger, *Sci. Adv.*, 2020, **6**, eaaw9733.
33 F. Giavazzi, G. Savorana, A. Vailati and R. Cerbino, *Soft Matter*, 2016, **12**, 6588–6600.
34 J. A. Richards, V. A. Martinez and J. Arlt, *Soft Matter*, 2021, **17**, 3945–3953.
35 M. Reufer, V. A. Martinez, P. Schurtenberger and W. C. K. Poon, *Langmuir*, 2012, **28**, 4618–4624.
36 R. You and R. McGorty, *Rev. Sci. Instrum.*, 2021, **92**, 023702.
37 F. Giavazzi, P. Edera, P. J. Lu and R. Cerbino, *Eur. Phys. J. E: Soft Matter Biol. Phys.*, 2017, **40**, 97.
38 H. Holthoff, S. U. Egelhaaf, M. Borkovec, P. Schurtenberger and H. Sticher, *Langmuir*, 1996, **12**, 5541–5549.
39 H. Holthoff, A. Schmitt, A. Fernandez-Barbero, M. Borkovec, M. Cabrerizo-Vilchez, P. Schurtenberger and R. Hidalgo-Alvarez, *J. Colloid Interface Sci.*, 1997, **192**, 463–470.
40 G. Trefalt, I. Szilagyi, T. Oncsik, A. Sadeghpour and M. Borkovec, *Chimia*, 2013, **67**, 772–776.
41 S. Xu and Z. Sun, *Soft Matter*, 2011, **7**, 11298–11308.
42 M. Elimelech, J. Gregory, X. Jia and R. A. Williams,*Particle Deposition and Aggregation: Measurement, Modelling, and Simulation*, Butterworth-Heinemann, 1998.
43 H. Reerink and J. T. G. Overbeek, *Discuss. Faraday Soc.*, 1954, **18**, 74–84.

44 J. Dumpler, *Heat Stability of Concentrated Milk Systems*, Springer, Fachmedien Wiesbaden, 2018.
45 R. Cerbino and A. Vailati, *Curr. Opin. Colloid Interface Sci.*, 2009, **14**, 416–425.
46 F. Giavazzi, D. Brogioli, V. Trappe, T. Bellini and R. Cerbino, *Phys. Rev. E: Stat., Nonlinear, Soft Matter Phys.*, 2009, **80**, 031403.
47 C. G. de Kruif, *J. Dairy Sci.*, 1998, **81**, 3019–3028.
48 S. Nöbel, K. Weidendorfer and J. Hinrichs, *J. Colloid Interface Sci.*, 2012, **386**, 174–180.
49 J. J. Crassous, L. Casal-Dujat, M. Medebach, M. Obiols-Rabasa, R. Vincent, F. Reinhold, V. Boyko, I. Willerich, A. Menzel, C. Moitzi, B. Reck and P. Schurtenberger, *Langmuir*, 2013, **29**, 10346–10359.
50 E. R. Weeks and D. A. Weitz, *Chem. Phys.*, 2002, **284**, 361–367.
51 L. Dahbi, M. Alexander, V. Trappe, J. K. G. Dhont and P. Schurtenberger, *J. Colloid Interface Sci.*, 2010, **342**, 564–570.
52 Z. Gaygadzhiev, M. Corredig and M. Alexander, *Langmuir*, 2008, **24**, 3794–3800.
53 S. Sandra, C. Cooper, M. Alexander and M. Corredig, *Food Res. Int.*, 2011, **44**, 951–956.
54 C. Beenakker and P. Mazur, *Phys. A*, 1983, **120**, 388–410.
55 C. Beenakker and P. Mazur, *Phys. A*, 1984, **126**, 349–370.
56 R. Gebhardt, W. Doster and U. Kulozik, *Braz. J. Med. Biol. Res.*, 2005, **38**, 1209–1214.
57 R. Gebhardt, N. Takeda, U. Kulozik and W. Doster, *J. Phys. Chem. B*, 2011, **115**, 2349–2359.
58 M. Sidoryk-Wegrzynowicz, K. Adamiak and L. Strużyńska, *Int. J. Mol. Sci.*, 2024, **25**, 12448.
59 S. Salimi, P.-L. Latreille, M. Le Goas, D. C. Boffito, J. Arlt, V. A. Martinez and X. Banquy, *Nano Today*, 2024, **56**, 102239.
60 V. Kumar, N. Sami, T. Kashav, A. Islam, F. Ahmad and M. I. Hassan, *Eur. J. Med. Chem.*, 2016, **124**, 1105–1120.

